

Article

Effect of Fluoride on the Morphology and Electrochemical Property of Co_3O_4 Nanostructures for Hydrazine Detection

Tuantuan Zhou ¹ , Wanlin Gao ¹, Qiang Wang ^{1,*} and Ahmad Umar ^{2,*}

¹ College of Environmental Science and Engineering, Beijing Forestry University, 35 Qinghua East Road, Haidian District, Beijing 100083, China; tuantuanzhou@bjfu.edu.cn or ztuant86@126.com (T.Z.); gaowanlin2016@bjfu.edu.cn (W.G.)

² Department of Chemistry, College of Science and Arts, and Promising Centre for Sensors and Electronic Devices (PCSED), Najran University, Najran 11001, Saudi Arabia

* Correspondence: qiangwang@bjfu.edu.cn (Q.W.); ahmadumar786@gmail.com (A.U.); Tel.: +86-136-9913-0626 (Q.W.); Tel: +966-534574597 (A.U.)

Received: 26 December 2017; Accepted: 19 January 2018; Published: 29 January 2018

Abstract: In this paper, we systematically investigated the influence of fluoride on the morphology and electrochemical property of Co_3O_4 nanostructures for hydrazine detection. The results showed that with the introduction of NH_4F during the synthesis process of Co_3O_4 , both $\text{Co}(\text{CO}_3)_{0.5}(\text{OH})\cdot 0.11\text{H}_2\text{O}$ and $\text{Co}(\text{OH})\text{F}$ precursors would be generated. To understand the influence of F on the morphology and electrochemical property of Co_3O_4 , three Co_3O_4 nanostructures that were respectively obtained from bare $\text{Co}(\text{CO}_3)_{0.5}(\text{OH})\cdot 0.11\text{H}_2\text{O}$, $\text{Co}(\text{OH})\text{F}$ and $\text{Co}(\text{CO}_3)_{0.5}(\text{OH})\cdot 0.11\text{H}_2\text{O}$ mixtures and bare $\text{Co}(\text{OH})\text{F}$ were successfully synthesized. The electrochemical tests revealed the sensing performance of prepared Co_3O_4 nanostructures decreased with the increase in the fluoride contents of precursors. The more that dosages of NH_4F were used, the higher crystallinity and smaller specific surface area of Co_3O_4 was gained. Among these three Co_3O_4 nanostructures, the Co_3O_4 that was obtained from bare $\text{Co}(\text{CO}_3)_{0.5}(\text{OH})\cdot 0.11\text{H}_2\text{O}$ -based hydrazine sensor displayed the best performances, which exhibited a great sensitivity ($32.42 \mu\text{A}\cdot\text{mM}^{-1}$), a low detection limit ($9.7 \mu\text{M}$), and a wide linear range ($0.010\text{--}2.380 \text{ mM}$), together with good selectivity, great reproducibility and longtime stability. To the best of our knowledge, it was revealed for the first time that the sensing performance of prepared Co_3O_4 nanostructures decreased with the increase in fluoride contents of precursors.

Keywords: cobalt oxide; fluoride; precursor; crystallinity; electrochemical activity

1. Introduction

Hydrazine and based chemicals are water soluble volatile colorless liquids, and the simplest unique diamine in its class has aroused wide concern for its large number of applications in many spheres, for instance, corrosive inhibitors, fuel cells and so on [1–4]. The laboratory research and commercial application of hydrazine as a reducing agent and catalyst are commonly implemented. However, hydrazine and its derivatives do great harm to the body through the digestive system along with skin permeation [5]. Consequently, it is highly imperative to propose a sensitive, original and analytically credible tool for the effective detection of hydrazine. Recently, electroanalytical techniques have developed as a desirable method for detection of many chemicals, such as hydroquinone [6], acetone [7], herbicides [8], etc. due to their great sensitivity, better efficiency and low cost. It is promising to develop electrochemical methods for hydrazine detection. Nowadays, lots of semiconductor metal oxides have been used for hydrazine electrochemical sensing. Ahmad et al. have fabricated a ZnO nanorods-based hydrazine sensor and showed a low detection limit [9]. Wu et al.

used MnO₂ nanoflowers for hydrazine detection and exhibited a high sensitivity [10]. However, the study on Co₃O₄ utilized for hydrazine is rare to report.

Cobaltous oxide (Co₃O₄), a kind of vital transition-metal oxide semiconductor with direct optical band gaps at 2.19 eV [11], has undergone extensive exploration recently for its wide-ranging potential applications as a gas sensor [12–14], catalyst [15–18], magnetic material [19], solar-energy absorber [20], supercapacitors and rechargeable lithium-ion-battery materials [21–24]. More significantly, because of its high catalytic performance, nanostructured Co₃O₄ is widely considered to be an attractive modified electrode material that can enhance the rate of electron transfer and minimize its over potential [25]. Up to now, various synthetic protocols have been developed for the synthesis of Co₃O₄ with diverse morphologies and designed nanostructures. Among them, a two-step approach, where co-based intermediates, such as Co(OH)₂ and (Co(CO₃)_{0.5}(OH)·0.11H₂O), are first fabricated by thermal annealing exposed to air, as the control on the morphologies of these intermediates has been widely used. However, for certain synthesis procedures, NH₄F was normally used during the synthesis step, because F is a good complexing ligand for Co²⁺. In the presence of F[−], CoF⁺ complex can firstly be formed to prevent Co(OH)₂ generation, which would make the morphology controllable [26,27]. Meanwhile, F may also lead to the formation of (Co(OH)F), which may cause the generation of impurities in the products. Up to now, the influence of F content on the formation and electrochemical performance of Co₃O₄ has not been clarified.

Thus, in this paper, the influence of fluoride (F) on the morphological and electrochemical performance of Co₃O₄ for hydrazine sensing was systematically investigated for the first time. Three types of Co₃O₄ samples were synthesized by thermal treatment of their precursors, which contain different amounts of F. The physical and chemical compositions of all constructed materials were systematically investigated. The electrochemical activity of these Co₃O₄ were comprehensively compared using cyclic voltammetry and amperometric response analysis.

2. Results and Discussion

2.1. Structural and Morphological Studies

The composition of the prepared precursors was first examined by XRD characterization. As shown in Figure 1a,c, all of the diffraction peaks could be well indexed to Co(CO₃)_{0.5}(OH)·0.11H₂O (JCPDS card No. 48-0083) and Co(OH)F (JCPDS card No. 50-0827), respectively, and no other peak could be found from the XRD patterns. Figure 1b verifies that the precursor powders are the mixture of Co(CO₃)_{0.5}(OH)·0.11H₂O and Co(OH)F. Furthermore, the characteristic peaks at 17.5°, 24.2°, 26.8°, 28.8°, 35.5°, 59.9°, and 62.2° can be indexed to the reflections of (020), (111), (220), (121), (040), (340), (412), and (450) planes of Co(CO₃)_{0.5}(OH)·0.11H₂O; while the characteristic peaks at 20.8°, 32.3°, 33.5°, 38.8°, 51.9°, 52.8°, and 57.0° can be indexed to the reflections of (110), (310), (201), (211), (221), (420), (511) planes of Co(OH)F. For the synthesis of Co₃O₄, all these three precursors were thermally annealed at 400 °C for 5 h in air. Figure 1d–f clearly indicate that all the diffraction peaks are well-assigned to the standard diffraction pattern of Co₃O₄ (JCPDS card No. 43-1003), which indicates that the precursors had been thoroughly converted to Co₃O₄ phase and there were no other impurities that could be detected. The crystallinity of the prepared products was evaluated via the Formula (1).

$$X_c = I_c / (I_c + KI_a) \times 100\% \quad (1)$$

In Formula (1), X_c represents the crystallinity measured by X-ray diffractometry; I_c is the integral intensity of the crystal diffraction peak; and I_a is the integral intensity of the amorphous diffuse peak; K is the relative scattering factor.

The crystallinity of prepared Co₃O₄ samples is calculated and shown in Table 1. It is obvious that Co₃O₄-1 possesses the lowest crystallinity (73.87%) and Co₃O₄-3 has the highest crystallinity 91.62%. To explore the influence of F on the crystallinity of Co₃O₄, different dosages of NH₄F (from 0 to 20 mmol) had been added during the synthesis process of Co₃O₄. As shown in Table 1, the crystallinity

of Co_3O_4 presents an increase trend with increasing the amount of NH_4F during the synthesis process of precursors, which indicates that the strong interaction between Co^{2+} and F^- can make the particles grow regularly.

The formation of the precursors and annealed products can be illustrated with the following steps. When $\text{CO}(\text{NH}_2)_2$ is used as a hydrolysis reagent, the formation process of $\text{Co}(\text{CO}_3)_{0.5}(\text{OH})\cdot 0.11\text{H}_2\text{O}$ can be depicted as Equations (2)–(4). While when HMT is used as a hydrolysis reagent, with the existence of F^- , the formation of $\text{Co}(\text{OH})\text{F}$ can be possibly expressed by Equations (5)–(8). After calcination, both of the precursors can be converted into cobaltic oxide by Equations (9) and (10).

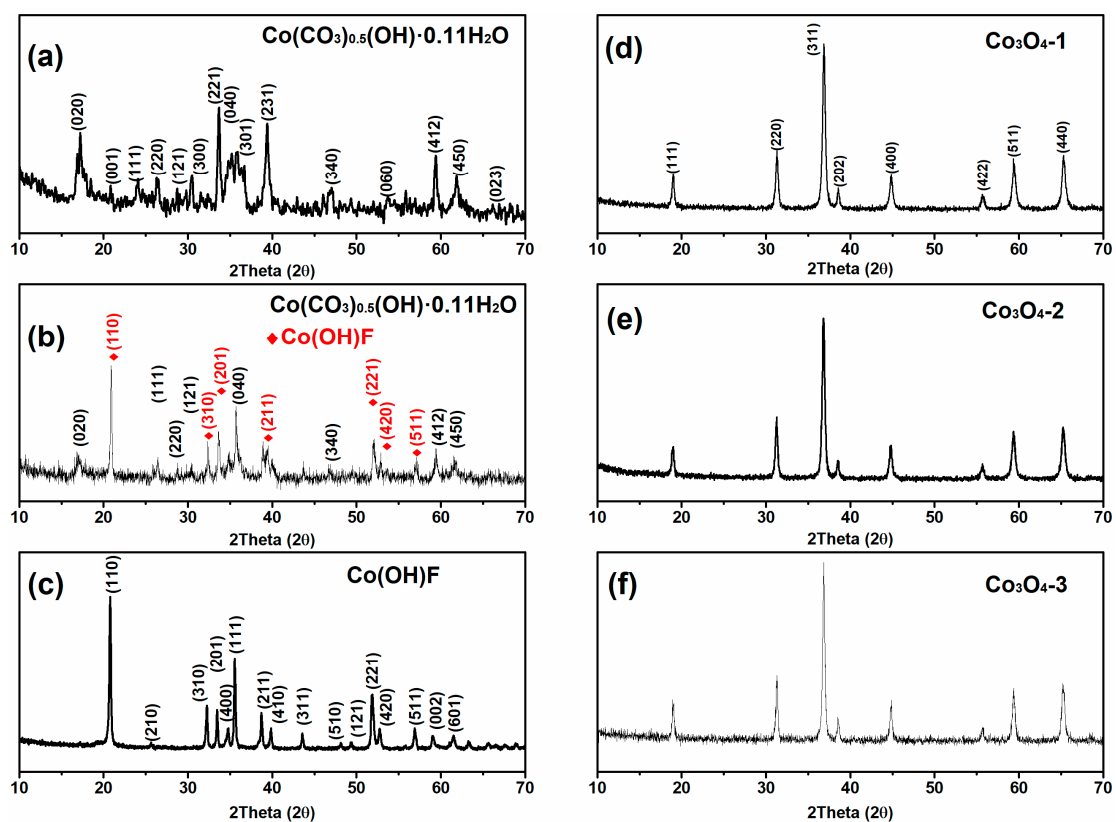
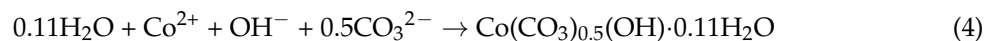
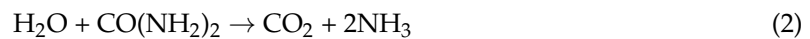


Figure 1. XRD patterns of (a) $\text{Co}(\text{CO}_3)_{0.5}(\text{OH})\cdot 0.11\text{H}_2\text{O}$; (b) $\text{Co}(\text{CO}_3)_{0.5}(\text{OH})\cdot 0.11\text{H}_2\text{O}$ and $\text{Co}(\text{OH})\text{F}$ mixture; (c) $\text{Co}(\text{OH})\text{F}$; (d) Co_3O_4 -1; (e) Co_3O_4 -2 and (f) Co_3O_4 -3.

Table 1. Synthesis of Co₃O₄ nanocrystals with different addition of NH₄F.

Raw Materials (mmol)			Precursor	Calcination (400 °C)	Crystallinity (%)	SSA (m ² ·g ⁻¹)
Co(NO ₃) ₂	NH ₄ F	CO(NH ₂) ₂				
5	0	10	P1 ¹	Co ₃ O ₄ -1	73.87	25.83
5	5	10	P1 and P2	Co ₃ O ₄	80.34	21.20
5	10	10	P1 and P2	Co ₃ O ₄ -2	84.24	18.44
5	15	10	P1 and P2	Co ₃ O ₄	88.05	14.55
5	20	10	P1 and P2	Co ₃ O ₄	90.46	12.44
5	20	HMT	P2 ¹	Co ₃ O ₄ -3	91.62	10.57

¹ P1 and P2 represents Co(CO₃)_{0.5}(OH)·0.11H₂O and Co(OH)F, respectively.

The FT-IR study also affirms the formation of precursors and the final Co₃O₄ samples. Figure 2 exhibits the FTIR spectra of Co₃O₄-1, Co₃O₄-2, and Co₃O₄-3, and their corresponding precursors. For the precursor of Co₃O₄-1, whose chemical composition is Co(CO₃)_{0.5}(OH)·0.11H₂O, the peaks at 3500 and 3379 cm⁻¹ are respectively ascribed to the O–H stretching mode of H₂O and the bond between O–H groups and CO₃²⁻. The bands observed at 1538 and 1340 cm⁻¹ are assigned to stretching vibration $\nu(\text{OCO}_2)$ and $\nu(\text{CO}_3)$ respectively. However, compared with another two curves, to some extent, the strength of $\nu(\text{OCO}_2)$ and $\nu(\text{CO}_3)$ is weakened with the presence of Co(OH)F. The remaining weak peaks at 1068, 835, 733 and 695 cm⁻¹ can respectively be $\nu(\text{C}=\text{O})$, $\delta(\text{CO}_3)$, $\delta(\text{OCO})$, and $\rho(\text{OCO})$ [28–31]. The peaks that appeared at 963 and 511 cm⁻¹ are ascribed to $\delta(\text{Co}-\text{OH})$ and $\rho_w(\text{Co}-\text{OH})$ bending modes, respectively [28–31]. For the precursor of Co₃O₄-3, whose chemical composition is Co(OH)F, the peak at 3575 cm⁻¹ is assigned to the O–H stretching mode too. The shoulder vibration at 3417 cm⁻¹ corresponds to the O–H groups interacting with fluoride anions. In addition, no any other band related to carbonate anions can be found (Figure 2a). After annealing treatment, the bands of precursors disappear and two very strong peaks are centered at 665 and 543 cm⁻¹ characteristic of Co₃O₄ are noticed (Figure 2b). The former peak at 665 cm⁻¹ corresponds to Co²⁺–O bond [30]. The other peak at 543 cm⁻¹ can be ascribed to Co³⁺–O bond [31]. The results verified the formation of Co₃O₄ under thermal degradation, which coincides with the XRD patterns.

To get more information about the chemical states of elements in prepared Co₃O₄ samples, XPS analysis was then performed. Figure 3a shows the Co 2p peaks of Co₃O₄-1, Co₃O₄-2, and Co₃O₄-3, respectively. The curve of Co 2p shows two spin-orbit doublets of Co 2p_{1/2} at 779.96 and 794.94 eV attributed to Co³⁺, and two spin-orbit doublets of Co 2p_{3/2} at 781.46 and 796.46 eV belonging to Co²⁺. The intensity of the peaks shows downward course from Co₃O₄-1 to Co₃O₄-3. Figure 3b depicts the O1s spectra of the prepared Co₃O₄ samples, the large O 1s peak at 530.12 eV is attributed to the lattice oxygen (LO) in Co₃O₄ crystals and the small O 1s peak at 531.47 eV represents the oxygen vacancies (OV) on the surface of Co₃O₄ [32–34]. The intensity of the oxygen vacancy also shows a decreased trend from Co₃O₄-1 to Co₃O₄-3 (Table 2). The more oxygen vacancies indicate a higher possibility for the exposure of active sites [35].

Table 2. XPS data of Co and O species of Co₃O₄ derived from different precursors.

Sample	Amount of Oxygen Species			
	Oxygen Vacancy (OV)		Lattice Oxygen (LO)	
	at. %	BE (eV)	at. %	BE (eV)
Co ₃ O ₄ -1	44.9	530.12	55.1	531.47
Co ₃ O ₄ -2	43.8	530.12	56.2	531.47
Co ₃ O ₄ -3	41.8	530.12	58.2	531.47

The general morphology of the precursors and the obtained Co₃O₄ products was further explored using FE-SEM, as shown in Figure 4. The Co(CO₃)_{0.5}(OH)·0.11H₂O precursor exhibited a nanorod structure, with a smooth surface (Figure 4a). The average length of the nanorods is in

the range of 3–5 μm . The $\text{Co}(\text{OH})\text{F}$ precursor showed gear-like nanosheets, with an uneven surface (Figure 4e). The average thickness of $\text{Co}(\text{OH})\text{F}$ nanosheets is about 0.025 μm and the typical diameter of the nanosheets is in the range of 8–12 μm . Figure 4b depicts the SEM image of the mixture of $\text{Co}(\text{CO}_3)_{0.5}(\text{OH})\cdot 0.11\text{H}_2\text{O}$ nanorods and $\text{Co}(\text{OH})\text{F}$ nanosheets. When $\text{CO}(\text{NH}_2)_2$ was used as the hydrolysis reagent, both $\text{Co}(\text{CO}_3)_{0.5}(\text{OH})\cdot 0.11\text{H}_2\text{O}$ and $\text{Co}(\text{OH})\text{F}$ precursors were generated in the same time with the existence of F. However, from Figure 4c, it is noteworthy that the quantity of nanorods is far more than nanosheets, which indicates that the growth rate of $\text{Co}(\text{CO}_3)_{0.5}(\text{OH})\cdot 0.11\text{H}_2\text{O}$ is faster than the growth rate of $\text{Co}(\text{OH})\text{F}$. The elemental mapping analysis in the selected area of Figure 4c further confirmed the generation of $\text{Co}(\text{OH})\text{F}$. Figure 5 suggests that the F element was evenly dispersed within the $\text{Co}(\text{OH})\text{F}$ sample, with a calculated atomic amount of ca. 5.8%. After annealing the precursors, the morphology of obtained Co_3O_4 -1, Co_3O_4 -2, and Co_3O_4 -3 samples were also characterized using FE-SEM, as shown in Figure 4b,d,f. It was worthwhile mentioning that the products still maintained the similar morphology with their precursors after the annealing treatment. Contrary to the precursors, the Co_3O_4 displayed rough and porous surfaces, which might be due to the abscission of attached OH ions during the calcination process. The difference of morphology may lead to the difference of specific surface area of Co_3O_4 . Based on the BET data, it could be found that the rod-like Co_3O_4 possessed larger specific surface area than sheet-like Co_3O_4 . The relatively large specific surface area of rod-like structure may be beneficial to the exposure of active sites and in the meantime facilitate the contact of Co_3O_4 to the targeted chemicals.

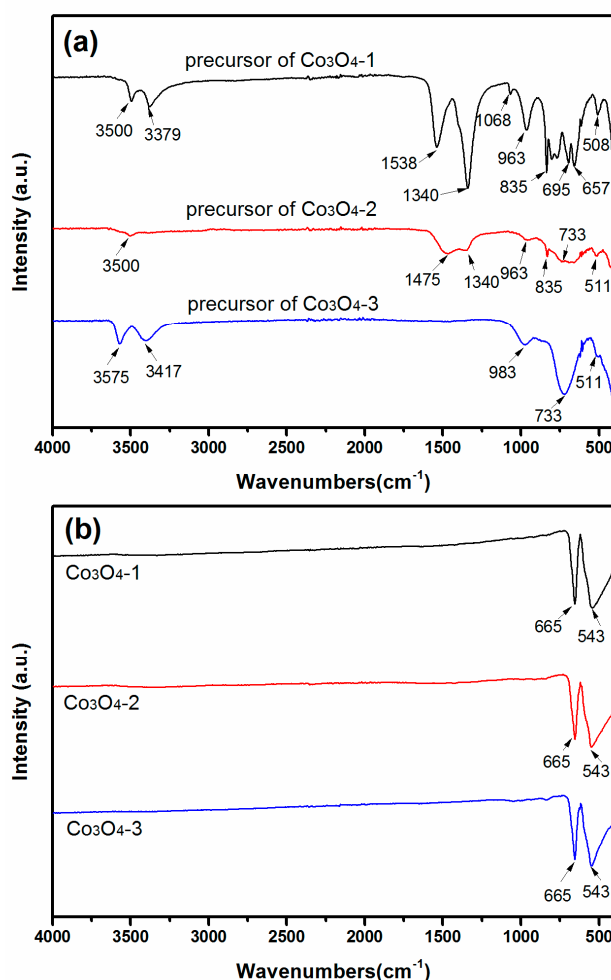


Figure 2. Typical FTIR spectra of the (a) precursors and (b) obtained Co_3O_4 products.

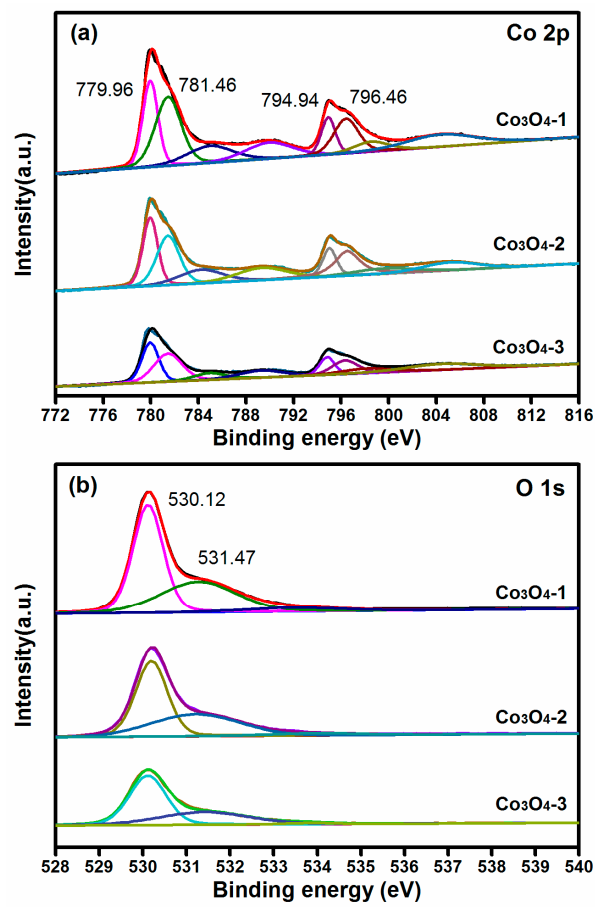


Figure 3. XPS analyses of (a) Co 2p and (b) O 1s for Co₃O₄-1, Co₃O₄-2 and Co₃O₄-3 nanocrystals.

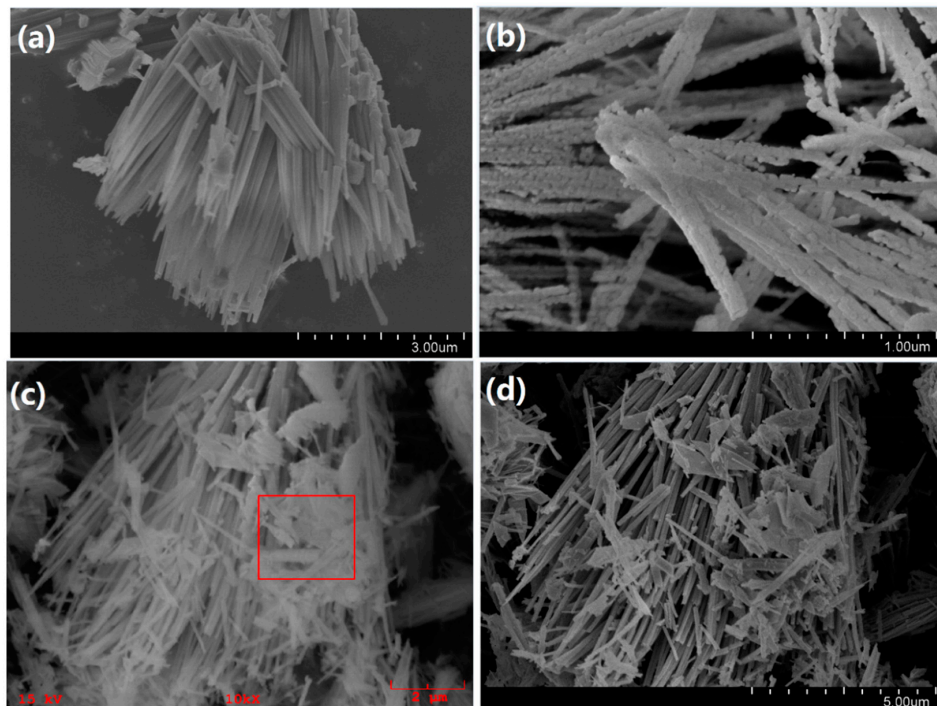


Figure 4. Cont.

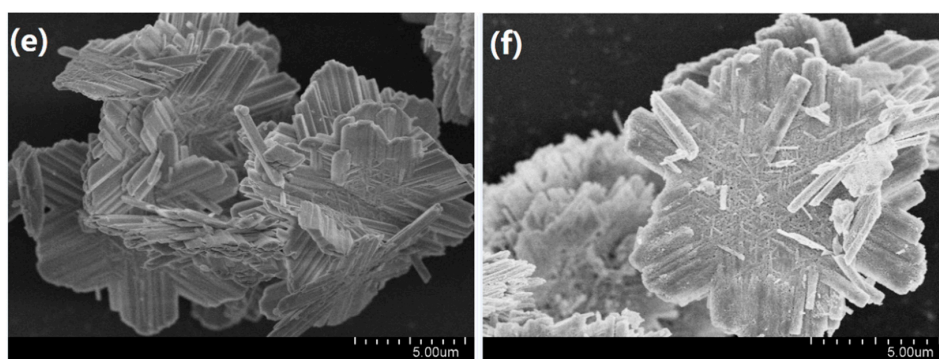


Figure 4. Typical FE-SEM images of (a) $\text{Co}(\text{CO}_3)_{0.5}(\text{OH})\cdot 0.11\text{H}_2\text{O}$ precursor; (b) Co_3O_4 -1; (c) the mixture of $\text{Co}(\text{CO}_3)_{0.5}(\text{OH})\cdot 0.11\text{H}_2\text{O}$ and $\text{Co}(\text{OH})\text{F}$; (d) Co_3O_4 -2; (e) $\text{Co}(\text{OH})\text{F}$ precursor; and (f) Co_3O_4 -3.

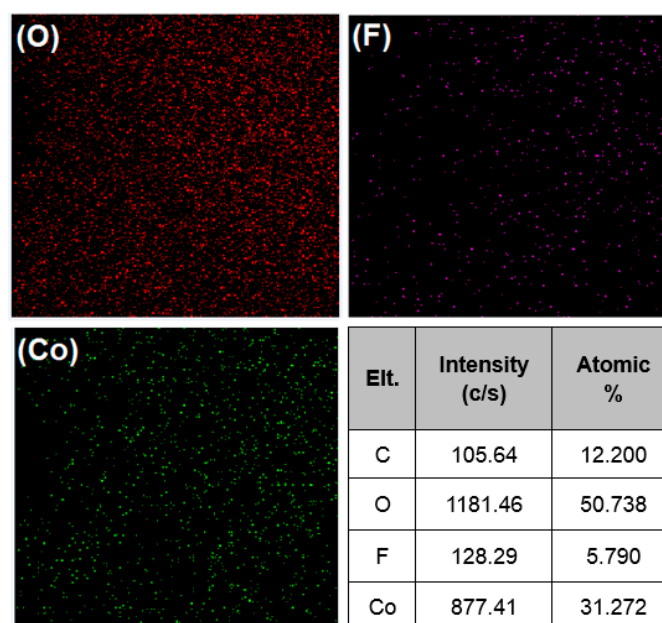


Figure 5. SEM-EDS elemental mapping (C, O, F, and Co) of the precursor of Co_3O_4 -2.

2.2. Hydrazine Chemical Sensor Studies of Co_3O_4 Modified Electrodes

To prepare the hydrazine sensor, Co_3O_4 nanomaterials were coated on the surface of GCE. The electrocatalytic activity of Co_3O_4 nanomaterials towards hydrazine was firstly investigated by cyclic voltammetry technique. Figure 6a shows the cyclic voltammogram (CV) of bare GCE and $\text{Co}_3\text{O}_4/\text{GCE}$ in the presence of 1 mM hydrazine in 0.1 M NaOH electrolyte at a scan rate of $0.02 \text{ V}\cdot\text{s}^{-1}$. It is apparent that no matter whether hydrazine exists, the bare GCE does not exhibit any redox peak in 0 to 0.6 V, just the current elevated when hydrazine added. This result indicates the low catalytic activity of bare GCE. However, for these three kinds of Co_3O_4 modified electrodes, there are significant differences among them. For Co_3O_4 -3 (obtained from $\text{Co}(\text{OH})\text{F}$) modified electrode, no peak could be observed when it was tested. However, for Co_3O_4 -2 (obtained from the mixture) and Co_3O_4 -1 (obtained from $\text{Co}(\text{CO}_3)_{0.5}(\text{OH})\cdot 0.11\text{H}_2\text{O}$) modified electrodes, an oxidation peak (I) apparently emerged at around 0.50 V. The observed CV response also exhibited reversible nature as it showed a reduction peak (II) at 0.46 V during the reverse sweep. Among them, Co_3O_4 -1 possesses the best electrochemical activity towards hydrazine oxidation while Co_3O_4 -3 has the poorest electrochemical activity towards hydrazine. This result suggests that F has a negative effect on the performance of Co_3O_4 . We believe

that the performance of Co_3O_4 should be related to their crystallinity and specific surface area. According to the XPS analysis, with increasing the amount of F in the synthesis process, the oxygen vacancy of their final product (Co_3O_4) shows a decreased trend. The addition of F allows the precursor to grow more regularly but cause the decrease of the specific surface area, resulting in relatively less active sites and worse performance of Co_3O_4 [36]. The possible reactions on Co_3O_4 electrode can be expressed as the following Equations (11)–(13).

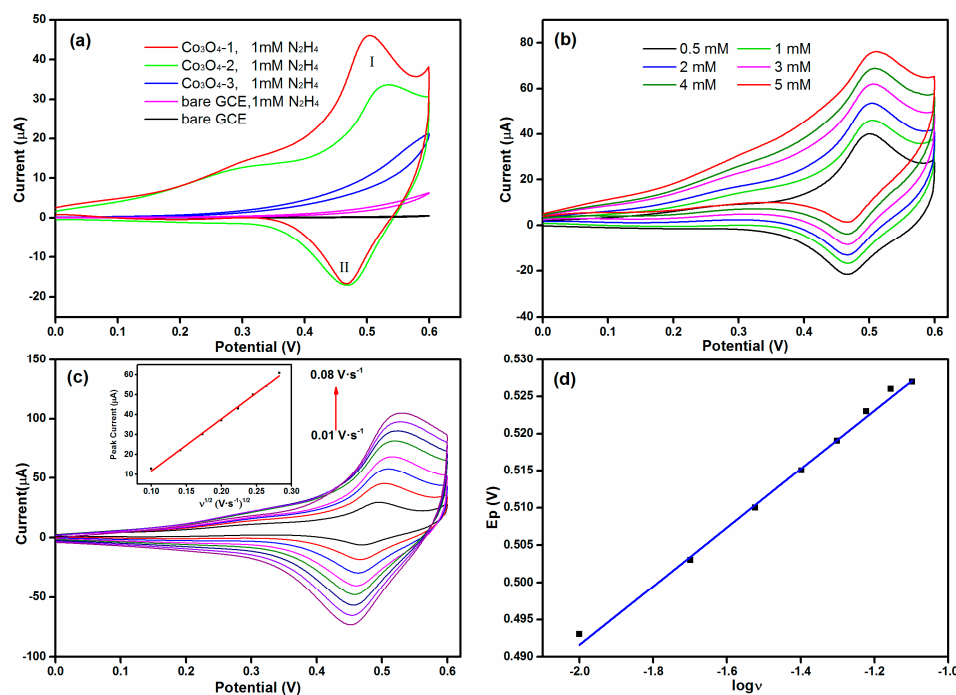
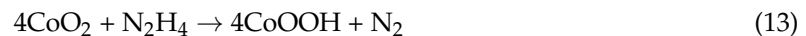
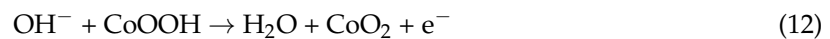
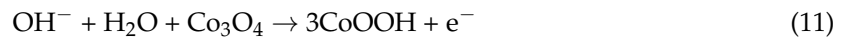


Figure 6. (a) Cyclic voltammograms for different modified electrodes in the presence of 1 mM hydrazine at a scan rate of $0.02 \text{ V}\cdot\text{s}^{-1}$; (b) Cyclic voltammograms of Co_3O_4 -1/GCE with different hydrazine concentrations at a scan rate of $0.02 \text{ V}\cdot\text{s}^{-1}$; (c) Cyclic voltammograms of Co_3O_4 -1/GCE with different scan rates (From 0.01 to 0.08), inset shows the anodic peak current vs. the square root of scan rate ($\nu^{1/2}$); and (d) the anodic peak potential (E_p) vs. $\log \nu$.

The influence of hydrazine concentration and the scan rates on the performance of modified electrode was then investigated using the Co_3O_4 -1 sample. Figure 6b exhibits the cyclic voltammograms of Co_3O_4 -1 modified GCE with different hydrazine concentrations at a scan rate of $0.02 \text{ V}\cdot\text{s}^{-1}$. With increasing the hydrazine concentration from 0.5 to 5 mM, the current displays a growth trend. The simultaneous response reveals that the fabricated Co_3O_4 -1-based sensor can be used for the effective determination of hydrazine. Figure 6c depicts the cyclic voltammograms of Co_3O_4 -1 modified GCE with 1 mM hydrazine at different scan rates ranging from 0.01 to $0.08 \text{ V}\cdot\text{s}^{-1}$. The inset of Figure 6c shows that the peak current (I_p) also increases synchronously with the scan rate. The relationship between I_p and the scan rate was further calculated based on the Randles–Sevcik equation [37]. The equation can be expressed as $I_p = 261.3 \nu^{1/2} - 14.4$ ($R^2 = 0.997$). The negative intercept may be due to the adsorption of the N_2H_4 occurred on the electrode surface, which indicates that the electrode reaction is not a single diffusion-controlled process [38]. Moreover, it is notable that

the peak potential shift towards positive potential with increasing the scan rate. Figure 6d exhibits the linear relation between the peak potential (E_p) and $\log(\nu)$, implying the irreversible oxidation of hydrazine at the surface of Co_3O_4 -1/GCE.

Figure 7a displays the chronoamperometric response of Co_3O_4 -1/GCE with different concentration of hydrazine. The transient currents decayed with prolonging the time, also revealing the diffusion-controlled process of hydrazine electrooxidation. The peak current exhibited linear relationship with $t^{-1/2}$ (Figure 7b). In addition, the slope of the line increased with increasing the hydrazine concentration (Figure 7c). Thus, the diffusion coefficient of hydrazine (D) could be calculated via Cottrell's equation:

$$I_p = nFAD^{1/2}C\pi^{-1/2}t^{-1/2} \quad (14)$$

In Equation (14), n , F ($\text{C}\cdot\text{mol}^{-1}$), A (cm^2), C ($\text{mol}\cdot\text{cm}^{-3}$) respectively represents the number of involved electron transfer, the Faraday constant (96,485), the surface area of GCE, and the dosage of hydrazine. The slopes of the obtained linear lines were plotted against the hydrazine concentrations (Figure 7c). Based on this plot, D was determined to be $1.66 \times 10^{-5} \text{ cm}^2\cdot\text{s}^{-1}$, which is consistent with the previous report [39].

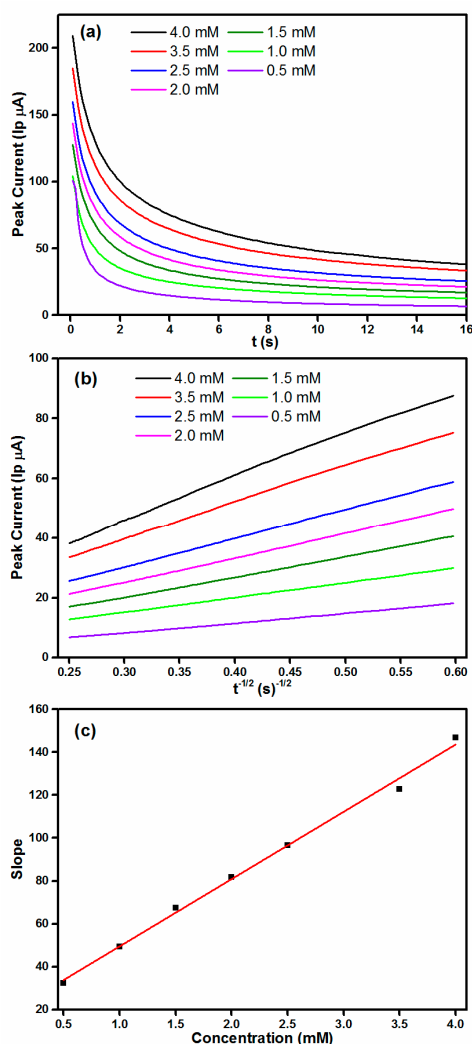


Figure 7. (a) Chronoamperograms obtained at Co_3O_4 -1/GCE with different concentrations of hydrazine in 0.1 M NaOH. Applied potential was 0.50 V; (b) Plot of current versus $t^{-1/2}$; and (c) The plot of slopes obtained from straight lines versus concentration of hydrazine.

2.3. Amperometric Detection of Hydrazine Using Co_3O_4 Modified Electrodes

The Co_3O_4 -1 and Co_3O_4 -2 modified electrodes were then used as a sensor for detection of hydrazine. The work potential was set at 0.50 V. For comparison, the amperometric responses of Co_3O_4 -1 and Co_3O_4 -2 electrodes are displayed. From Figure 8a,c, it is apparent that with the successive addition of hydrazine to a stirred solution, the anodic current increases gradually. When an aliquot of hydrazine was dropped into the stirred NaOH solution, the amperometric responses of the Co_3O_4 -1 modified electrode achieved a steady state within 2 s, which is faster than the Co_3O_4 -2 modified electrode. On the other hand, the magnitudes of the response current of the Co_3O_4 -1 modified electrode is also larger than the Co_3O_4 -2 modified electrode at the same condition. These results suggest that the Co_3O_4 -1 modified electrode has better electrochemical performance than the Co_3O_4 -2 modified electrode. When the hydrazine concentration exceeds a certain range, the response currents will no longer increase, but turn to be a declining trend. This phenomenon indicates that the hydrazine concentration exceeds the critical value of linear range. In order to further distinguish the difference between the two electrodes, mathematic fitting was utilized to calculate the sensitivity, linear response range and the detection limit. Figure 8b,d exhibit the liner relationship between hydrazine concentration and response current. For the Co_3O_4 -1 modified electrode, the equation can be explained as $I(\mu\text{A}) = 32.42 C(\text{mM}) - 0.69$ ($R^2 = 0.999$), while for the Co_3O_4 -2 modified electrode, the equation can be presented as $I(\mu\text{A}) = 25.28 C(\text{mM}) + 1.160$ ($R^2 = 0.999$). The plots also displayed a linear relationship with the hydrazine concentration in the range of 0.010 to 2.380 mM and 0.027 to 0.890 mM, respectively. For Co_3O_4 -1 and Co_3O_4 -2, the sensitivity that was found to be $32.42 \mu\text{A}\cdot\text{mM}^{-1}$ and $25.28 \mu\text{A}\cdot\text{mM}^{-1}$, respectively. The detection limit for the Co_3O_4 -1 and Co_3O_4 -2 fabricated hydrazine sensors were calculated to be $9.73 \mu\text{M}$ and $10.74 \mu\text{M}$ ($S/N = 3$).

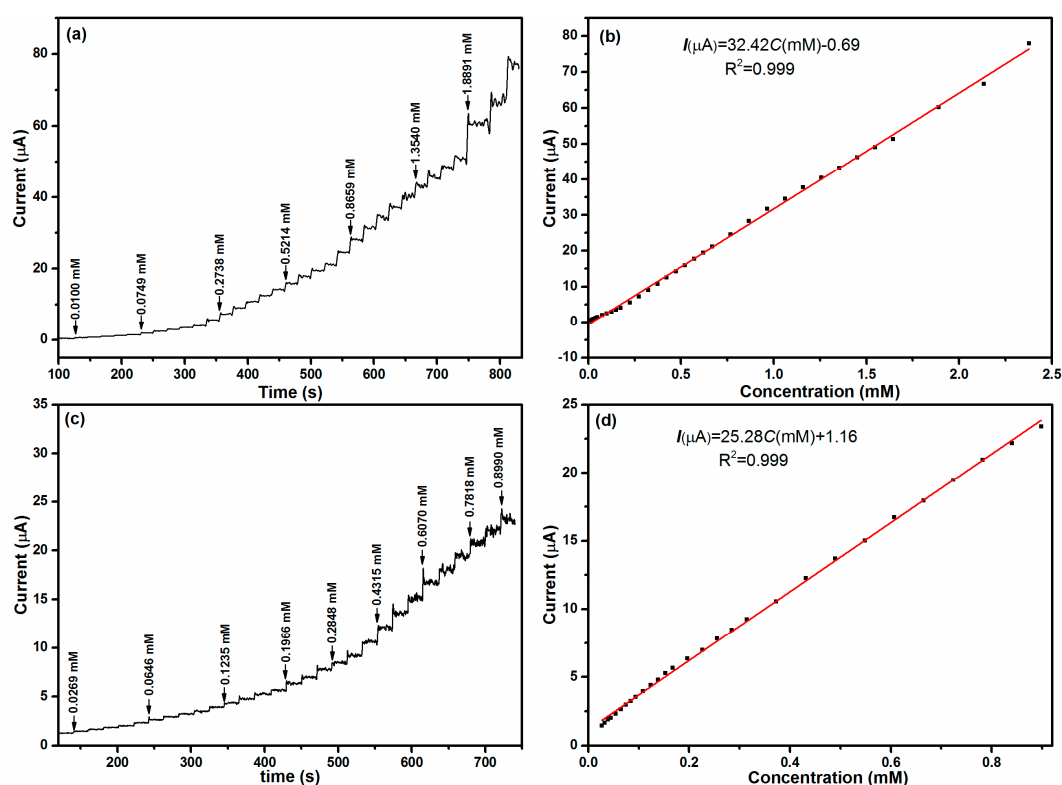


Figure 8. Amperometric responses of (a) Co_3O_4 -1 and (c) Co_3O_4 -2 modified electrodes with successive addition of hydrazine into 0.1 M NaOH; (b,d) the linear relationships between current vs. hydrazine concentration of Co_3O_4 -1 and Co_3O_4 -2 modified electrodes.

Table 3 summarizes the electrochemical parameters of some reported N_2H_4 sensors. Compared with them, the Co_3O_4 -1/GCE and Co_3O_4 -2/GCE exhibit rather high sensitivity and wide linear range. The performance of Co_3O_4 -1/GCE is better than Co_3O_4 -2/GCE. These results reveal that the existence of F in the synthesis of Co_3O_4 has a great impact on its electrochemical performance. To explore the influence of surface area of the obtained Co_3O_4 samples on their electrochemical performances, the surface area normalized current and sensitivity of Co_3O_4 -1 (obtained bare $Co(CO_3)_{0.5}(OH) \cdot 0.11H_2O$) and Co_3O_4 -2 (obtained the mixture of $Co(CO_3)_{0.5}(OH) \cdot 0.11H_2O$ and $Co(OH)F$) were shown as Table 4. The Co_3O_4 -1/GCE and Co_3O_4 -2/GCE exhibit no significant difference in surface area normalized current and surface area normalized sensitivity, which implies that the specific surface area is one of crucial factors for the electrochemical performances of Co_3O_4 . As above-mentioned, the amount of NH_4F is inversely related to the specific surface area. The dosage of NH_4F during the hydrothermal process affects the specific surface area of the products directly and therefore causes the difference in their electrochemical performances. To obtain the highly active Co_3O_4 -based modified electrodes for hydrazine detection, F should be avoided, although in many cases the F species cannot be detected by the XRD and FTIR analysis. However, the mechanism on how the remaining F affects the electrochemical activity of Co_3O_4 is still under investigation.

Table 3. Comparison of electrochemical parameters of various nanomaterials-based hydrazine sensor.

Electrode Materials	Sensitivity ($\mu A \cdot \mu M^{-1}$)	Detection Limit (μM)	Linear Range (mM)	Ref.
Ru-complex films	–	8.5	0.010–10	[40]
Nano-Au/Ti	1.117	42	0.5–4	[41]
Nickel tetrasulfonated phthalocyanine	0.0079	10	0.1–0.6	[42]
MWCNTs/Chlorogenic	$4.1 \mu A \cdot mM^{-1} \cdot cm^{-2}$	8	0.0025–0.5	[43]
GO/CTS/Pt	$104.6 \mu A \cdot mM^{-1} \cdot cm^{-2}$	3.6	0.02–1	[44]
Co_3O_4 -1	32.42	9.73	0.010–2.38	This work
Co_3O_4 -2	25.28	10.74	0.027–0.890	

Table 4. The surface area normalized current and sensitivity of the obtained Co_3O_4 samples.

Materials	Current (μA)	Sensitivity ($\mu A \cdot mM^{-1}$)	SSA ($m^2 \cdot g^{-1}$)	Surface Area Normalized Current ($\mu A \cdot m^{-2} \cdot g$)	Surface Area Normalized Sensitivity ($\mu A \cdot mM^{-1} \cdot m^{-2} \cdot g$)
Co_3O_4 -1	46.05	32.42	25.83	1.78	1.26
Co_3O_4 -2	33.58	25.28	18.44	1.81	1.37
Co_3O_4 -3	–	–	10.57	–	–

2.4. Selectivity, Reproducibility and Stability Tests

Selectivity and stability are two of key parameters to evaluate performance of chemical sensors. Thus, the selectivity and stability of the Co_3O_4 -1-based hydrazine sensor were also explored. Figure 9a exhibits the $i-t$ curve response of hydrazine and interferent (Cl^- , CO_3^{2-} , NO_3^- , NO_2^- , CH_3COO^- , K^+ , Na^+ , tap water, and humic acid). When 0.1 M N_2H_4 (10 μL) was injected to the NaOH solution, a quick response can be detected. However, when the same dosage of interfering species is added to the electrolyte, no obvious current response could be observed, suggesting the good selectivity of Co_3O_4 -1/GCE for N_2H_4 detection. To evaluate the reproducibility, seven different glassy carbon electrodes were prepared via the same modification step. The relative standard deviation value of peak current towards 1 mM hydrazine was found to be 7.23% (Figure 9b). To test the stability, the electrode was stored for five days in ambient conditions. Figure 9c displays the peak current of Co_3O_4 -1/GCE within five days. The value of peak current shows a declining trend with prolonging the time, but the peak current can still reach 86% of its initial response after being stored for five days. The obtained result suggests the long time stability of Co_3O_4 -1/GCE.

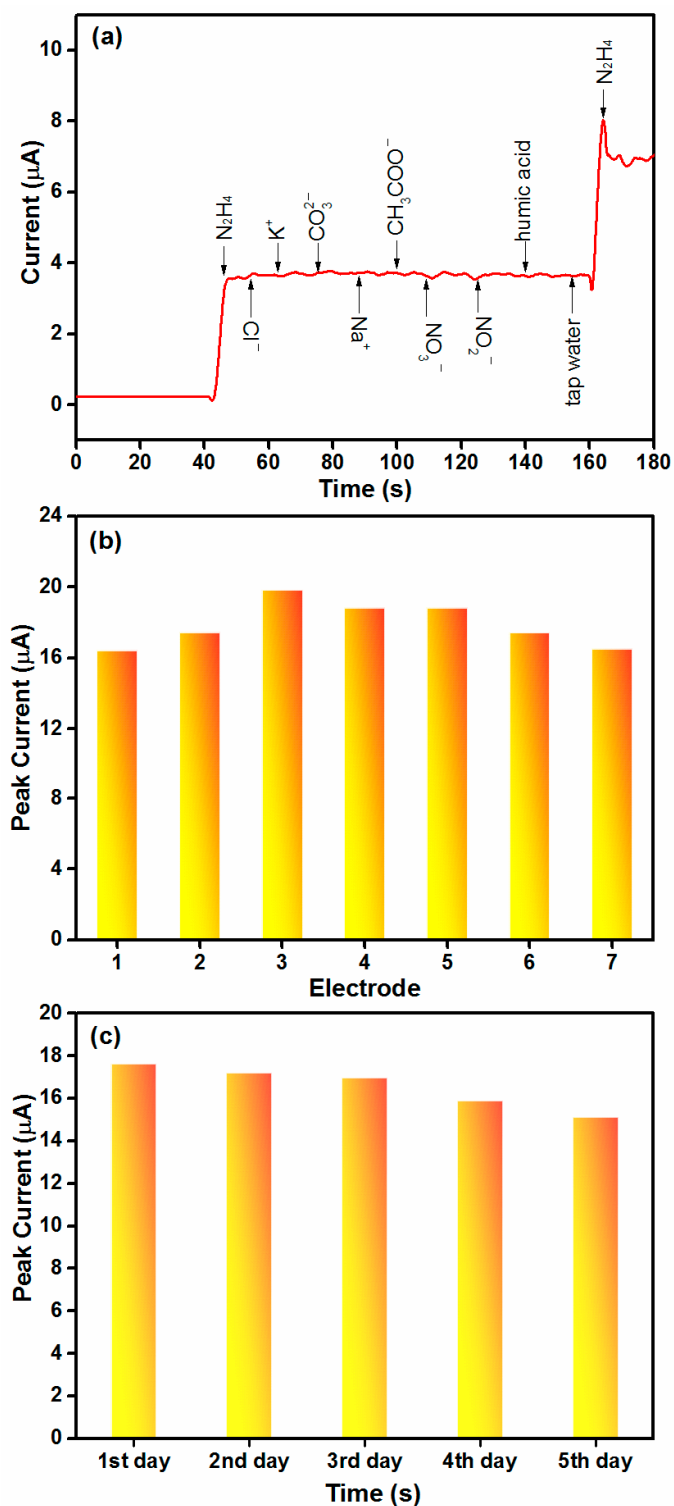


Figure 9. (a) The amperometric response to the addition of hydrazine with interfering species including Cl^- , CO_3^{2-} , NO_3^- , NO_2^- , CH_3COO^- , K^+ , Na^+ , tap water, and humic acid; (b) Peak currents of seven electrodes evaluated in 1 mM hydrazine; and (c) The peak current of Co_3O_4 -1/GCE after being stored at room temperature for five days.

2.5. Real Sample Test

In order to evaluate the validity of the proposed method, the Co_3O_4 -1/GCE was applied for the detection of hydrazine in different water samples which prepared by adding known amounts of hydrazine in water samples, the results are listed in Table 5. When a known amount of hydrazine was added to distilled water, tap water, and river water, quantitative recoveries of 99.77–102.79%, 98.33–101.63%, 98.63–99.30% were obtained respectively. All the results revealed the feasibility of the proposed electrode in the determination of hydrazine in water samples.

Table 5. The real sample analysis of Co_3O_4 -1-based hydrazine sensor using recovery method.

Sample	Hydrazine Added (μM)	Hydrazine Founded (μM)	Recovery
Distilled Water	10	10.28	102.79%
	20	19.98	99.88%
	50	49.88	99.77%
Tap Water	10	10.16	101.63%
	20	19.63	98.14%
	50	49.16	98.33%
River Water	10	9.86	98.63%
	20	19.51	97.56%
	50	49.65	99.30%

3. Materials and Methods

3.1. Synthesis of Co_3O_4 Nanostructures

All the precursors were synthesized using a straightforward hydrothermal process. The detailed synthesis procedures were described as follows. 1.455 g (5 mmol) of $\text{Co}(\text{NO}_3)_2 \cdot 6\text{H}_2\text{O}$ and 0.601 g (10 mmol) of $\text{CO}(\text{NH}_2)_2$ were mixed in 50 mL DI water and stirred continuously for 10 min. The obtained mixture solution was moved into a 100 mL autoclave and then hydrothermally at 95 °C for 24 h. The attained precipitates were concentrated via centrifugation, and repeatedly rinsed with absolute ethanol and distilled water and subsequently dried at 60 °C. The dried powder was the precursor for Co_3O_4 -1, being $\text{Co}(\text{CO}_3)_{0.5}(\text{OH}) \cdot 0.11\text{H}_2\text{O}$. The precursor for Co_3O_4 -2 was prepared using the similar way except extra addition 0.370 g (10 mmol) of NH_4F , being $\text{Co}(\text{CO}_3)_{0.5}(\text{OH}) \cdot 0.11\text{H}_2\text{O}$ and $\text{Co}(\text{OH})\text{F}$ mixture. The precursor for Co_3O_4 -3 was synthesized similarly to the precursor of Co_3O_4 -2 but changing the urea to hexamethylenetetramine ($\text{C}_6\text{H}_{12}\text{N}_4$, HMT), being pure $\text{Co}(\text{OH})\text{F}$. The detailed synthesized conditions are summarized in Table 1. To obtain the Co_3O_4 products, all the precursors were annealed at 400 °C for 4 h. For ease of description, the products obtained from bare $\text{Co}(\text{CO}_3)_{0.5}(\text{OH}) \cdot 0.11\text{H}_2\text{O}$, pure $\text{Co}(\text{OH})\text{F}$, and their mixture were designated as Co_3O_4 -1, Co_3O_4 -3, and Co_3O_4 -2, respectively.

3.2. Electrode Modification

Before modification, the prepared glassy carbon electrode (GCE) was respectively polished with 1.0, 0.3, 0.05 μm alumina powder for 10 min, and then rinsed with distilled water followed by drying under ambient conditions. The obtained homogeneous slurries containing 5 mg Co_3O_4 , 50 μL of Nafion solution (5 wt. %, DuPont 520, Wilmington, DE, USA), and 1 mL of ethanol was the mixture of all chemical together via sonication for 30 min. The Co_3O_4 modified GCE was produced by transferring 5 μL of the above attained homogeneous slurry on the GCE, and followed dried at ambient temperature.

3.3. Characterization of Samples

XRD spectra were acquired from Shimadzu XRD-7000 (Shimadzu, Kyoto, Japan) diffractometer ($2\theta = 10^\circ$ - 70°). Molecular speciation of the samples was examined by Bruker VERTEX 70 FT-IR spectrophotometer (Bruker, Billerica, MA, USA) in the range of 4000 – 400 cm^{-1} . XPS analysis was performed on a Thermo Scientific Escalab 250Xi instrument (Thermo Scientific, Waltham, MA, USA). The specific surface area (SSA) analysis was conducted by using Builder SSA-7000 (Beijing Builder Electronic Technology Co., Ltd, Beijing, China). SEM analysis was performed on a Hitachi SU8010 (Hitachi, Tokyo, Japan) field emission scanning microscope.

4. Conclusions

In summary, three types of Co_3O_4 samples were prepared and utilized as electrode materials for hydrazine detection. XRD analyses demonstrated that the precursors for Co_3O_4 -1, Co_3O_4 -2, and Co_3O_4 -3 were $\text{Co}(\text{CO}_3)_{0.5}(\text{OH})\cdot 0.11\text{H}_2\text{O}$, the mixture of $\text{Co}(\text{OH})\text{F}$ and $(\text{Co}(\text{CO}_3)_{0.5}(\text{OH})\cdot 0.11\text{H}_2\text{O})$, and $\text{Co}(\text{OH})\text{F}$, respectively. SEM analyses showed that these three Co_3O_4 samples possess different morphologies. The existence of F in their precursors was confirmed using SEM-EDS elemental mapping. Cyclic voltammetry results revealed that the electrochemical activity of Co_3O_4 decreased with the increase of F content in precursors. Furthermore, the prepared Co_3O_4 -1 and Co_3O_4 -2 were used to fabricate hydrazine chemical sensor. The results indicated that the Co_3O_4 -1-based hydrazine sensor possessed a high sensitivity of $32.42 \mu\text{A}\cdot\text{mM}^{-1}$, a low detection limit of $9.7 \mu\text{M}$ ($S/N = 3$), and a wide linear range from 0.010 to 2.380 mM . All these observed parameters were much better than those of the Co_3O_4 -2 or Co_3O_4 -3-based hydrazine sensors. The obtained results show that the fabricated hydrazine sensor also has good selectivity, great reproducibility and longtime stability.

Acknowledgments: This work was supported by the Fundamental Research Funds for the Central Universities (2016ZCQ03), and the Beijing Excellent Young Scholar (2015000026833ZK11). Ahmad Umar would like to acknowledge the Ministry of Higher Education, Kingdom of Saudi Arabia for the research grant under the Promising Centre for Sensors and Electronic Devices (PCSED) at Najran University.

Author Contributions: Qiang Wang and Ahmad Umar conceived and designed the experiments; Tuantuan Zhou performed the experiments and analyzed the data; Wanlin Gao and Ahmad Umar contributed reagents/materials/analysis tools; Tuantuan Zhou and Qiang Wang wrote the paper.

Conflicts of Interest: The authors declare no conflict of interest.

References

1. Ma, X.; Zhang, J.; Jiang, Q.; Liu, X.; Xu, W.; Zheng, M.; Hou, B. Highly Dispersed Ag/Graphene Composites with Enhanced Electro-Oxidation of Hydrazine. *Sci. Adv. Mater.* **2016**, *8*, 1305–1308. [[CrossRef](#)]
2. Patel, N.B.; Khan, I.H.; Rajani, S.D. Pharmacological evaluation and characterizations of newly synthesized 1, 2, 4-triazoles. *Eur. J. Med. Chem.* **2010**, *45*, 4293–4299. [[CrossRef](#)] [[PubMed](#)]
3. Ragnarsson, U. Synthetic methodology for alkyl substituted hydrazines. *Chem. Soc. Rev.* **2001**, *30*, 205–213. [[CrossRef](#)]
4. Al-Hadeethi, Y.; Al-Heniti, S.; Umar, A. Highly Sensitive Hydroquinone Chemical Sensor Based on $\text{Cd}_{0.5}\text{Mg}_{0.4}\text{Ca}_{0.1}\text{Fe}_2\text{O}_4$ Nanoparticles. *Sci. Adv. Mater.* **2017**, *9*, 2196–2201.
5. Tafazoli, S.; Mashregi, M.; O'Brien, P.J. Role of hydrazine in isoniazid-induced hepatotoxicity in a hepatocyte inflammation model. *Toxicol. Appl. Pharmacol.* **2008**, *229*, 94–101. [[CrossRef](#)] [[PubMed](#)]
6. Ansari, S.A.; Khatoun, Z.; Parveen, N.; Fouad, H.; Kulkarni, A.; Umar, A.; Ansari, Z.A.; Ansari, S.G. Polyaniline-Functionalized TiO_2 Nanoparticles as a Suitable Matrix for Hydroquinone Sensor. *Sci. Adv. Mater.* **2017**, *9*, 2032–2038.
7. Zhou, Q.; Hong, C.; Yao, Y.; Ibrahim, A.M.; Xu, L.; Kumar, R.; Talbala, S.M.; Kim, S.H.; Umar, A. Fabrication and characterization of highly sensitive acetone chemical sensor based on ZnO nanoballs. *Materials* **2017**, *10*, 799. [[CrossRef](#)] [[PubMed](#)]

8. Ebrahimiasl, S.; Seifi, R.; Nahli, R.E.; Zakaria, A. Ppy/Nanographene Modified Pencil Graphite Electrode Nanosensor for Detection and Determination of Herbicides in Agricultural Water. *Sci. Adv. Mater.* **2017**, *9*, 2045–2053.
9. Ahmad, R.; Tripathy, N.; Ahn, M.S.; Hahn, Y.B. Highly stable hydrazine chemical sensor based on vertically-aligned ZnO nanorods grown on electrode. *J. Colloid Interf. Sci.* **2017**, *494*, 153–158. [[CrossRef](#)] [[PubMed](#)]
10. Wu, J.; Zhou, T.; Wang, Q.; Umar, A. Morphology and chemical composition dependent synthesis and electrochemical properties of MnO₂-based nanostructures for efficient hydrazine detection. *Sens. Actuators B Chem.* **2016**, *224*, 878–884. [[CrossRef](#)]
11. Gulino, A.; Fiorito, G.; Fragalá, I. Deposition of thin films of cobalt oxides by MOCVD. *J. Mater. Chem.* **2003**, *13*, 861–865. [[CrossRef](#)]
12. Patil, D.; Patil, P.; Subramanian, V.; Joy, P.A.; Potdar, H.S. Highly sensitive and fast responding CO sensor based on Co₃O₄ nanorods. *Talanta* **2010**, *81*, 37–43. [[CrossRef](#)] [[PubMed](#)]
13. Wen, Z.; Zhu, L.; Li, Y.; Zhang, Z.; Ye, Z. Mesoporous Co₃O₄ nanoneedle arrays for high-performance gas sensor. *Sens. Actuators B Chem.* **2014**, *203*, 873–879. [[CrossRef](#)]
14. Vetter, S.; Haffer, S.; Wagner, T.; Tiemann, M. Nanostructured Co₃O₄ as a CO gas sensor: Temperature-dependent behavior. *Sens. Actuators B Chem.* **2015**, *206*, 133–138. [[CrossRef](#)]
15. Liang, Y.; Li, Y.; Wang, H.; Zhou, J.; Wang, J.; Regier, T.; Dai, H. Co₃O₄ nanocrystals on graphene as a synergistic catalyst for oxygen reduction reaction. *Nat. Mater.* **2011**, *10*, 780–786. [[CrossRef](#)] [[PubMed](#)]
16. Liu, Q.Y.; Yang, F.; Liu, Z.H.; Li, G. Preparation of SnO₂-Co₃O₄/C biochar catalyst as a Lewis acid for corncob hydrolysis into furfural in water medium. *J. Ind. Eng. Chem.* **2015**, *26*, 46–54. [[CrossRef](#)]
17. Zeng, T.; Zhang, X.; Wang, S.; Niu, H.; Cai, Y. Spatial confinement of a Co₃O₄ catalyst in hollow metal-organic frameworks as a nanoreactor for improved degradation of organic pollutants. *Environ. Sci. Technol.* **2015**, *49*, 2350–2357. [[CrossRef](#)] [[PubMed](#)]
18. Kim, S.; Kim, K.H.; Bark, C.W. Two-Dimensional Nanomaterials: Their Structures, Synthesis, and Applications. *Sci. Adv. Mater.* **2017**, *9*, 1441–1457. [[CrossRef](#)]
19. Benitez, M.J.; Petravic, O.; Salabas, E.L.; Radu, F.; Tüysüz, H.; Schüth, F.; Zabel, H. Evidence for core-shell magnetic behavior in antiferromagnetic Co₃O₄ nanowires. *Phys. Rev. Lett.* **2008**, *101*, 7206–7210. [[CrossRef](#)] [[PubMed](#)]
20. Ando, M.; Kadono, K.; Kamada, K.; Ohta, K. Third-order nonlinear optical responses of nanoparticulate Co₃O₄ films. *Thin Solid Films* **2004**, *446*, 271–276. [[CrossRef](#)]
21. Xiao, Y.; Liu, S.; Li, F.; Zhang, A.; Zhao, J.; Fang, S.; Jia, D. 3D hierarchical Co₃O₄ twin-spheres with an urchin-like structure: Large-scale synthesis, multistep-splitting growth, and electrochemical pseudocapacitors. *Adv. Funct. Mater.* **2012**, *22*, 4052–4059. [[CrossRef](#)]
22. Wang, H.; Xu, Z.; Yi, H.; Wei, H.; Guo, Z.; Wang, X. One-step preparation of single-crystalline Fe₂O₃ particles/graphene composite hydrogels as high performance anode materials for supercapacitors. *Nano Energy* **2014**, *7*, 86–96. [[CrossRef](#)]
23. Feng, C.; Zhang, J.; He, Y.; Zhong, C.; Hu, W.; Liu, L.; Deng, Y. Sub-3 nm Co₃O₄ nanofilms with enhanced supercapacitor properties. *ACS Nano* **2015**, *9*, 1730–1739. [[CrossRef](#)] [[PubMed](#)]
24. Kim, B.H.; Park, Y.K.; An, K.H.; Lee, H.; Jung, S.C. Impregnation of Cobalt on Graphene Sheet Using Liquid Phase Plasma Method for Lithium-Ion Batteries Application. *Sci. Adv. Mater.* **2016**, *8*, 1769–1773. [[CrossRef](#)]
25. Tahira, A.; Nafady, A.; Baloach, Q.; Sherazi, S.T.H.; Shaikh, T.; Arain, M.; Magnus, M.; Ibupoto, Z.H. Ascorbic acid assisted synthesis of cobalt oxide nanostructures, their electrochemical sensing application for the sensitive determination of hydrazine. *J. Electron. Mater.* **2016**, *45*, 3695–3701. [[CrossRef](#)]
26. Mei, W.; Huang, J.; Zhu, L.; Ye, Z.; Mai, Y.; Tu, J. Synthesis of porous rhombus-shaped Co₃O₄ nanorod arrays grown directly on a nickel substrate with high electrochemical performance. *J. Mater. Chem.* **2012**, *22*, 9315–9321. [[CrossRef](#)]
27. Zhu, L.; Wen, Z.; Mei, W.; Li, Y.; Ye, Z. Porous CoO nanostructure arrays converted from rhombic Co(OH)F and needle-like Co(CO₃)_{0.5}(OH)·0.11H₂O and their electrochemical properties. *J. Phys. Chem. C* **2013**, *117*, 20465–20473. [[CrossRef](#)]
28. Fang, Z.; Yu, H.; Dang, Y.; Gao, N.; Ma, N.; Peng, J.; Xie, K.; Li, L. Electrochemical and Printable Properties of Polydopamine Decorated Carbon Nanotube Ink. *Sci. Adv. Mater.* **2017**, *9*, 2039–2044.

29. Ngai, K.S.; Tan, W.T.; Zainal, Z.; Zawawi, R.M.; Juan, J.C. Electrochemical Sensor Based on Single-Walled Carbon Nanotube/ZnO Photocatalyst Nanocomposite Modified Electrode for the Determination of Paracetamol. *Sci. Adv. Mater.* **2016**, *8*, 788–796. [[CrossRef](#)]
30. Herrero, M.; Benito, P.; Labajos, F.M.; Nanosize, V.R. Cobalt oxide-containing catalysts obtained through microwave-assisted methods. *Catal. Today* **2007**, *128*, 129–137. [[CrossRef](#)]
31. Salavati-Niasari, M.; Davar, F.; Mazaheri, M.; Shaterian, M. Preparation of cobalt nanoparticles from [bis(salicylidene)cobalt(II)]-oleylamine complex by thermal decomposition. *J. Magn. Magn. Mater.* **2008**, *320*, 575–578. [[CrossRef](#)]
32. Tyuliev, G.; Angelov, S. The nature of excess oxygen in $\text{Co}_3\text{O}_{4+\epsilon}$. *Appl. Surf. Sci.* **1988**, *32*, 381–391. [[CrossRef](#)]
33. He, T.; Chen, D.; Jiao, X.; Wang, Y.; Duan, Y. Solubility-controlled synthesis of high-quality Co_3O_4 nanocrystals. *Chem. Mater.* **2005**, *17*, 4023–4030. [[CrossRef](#)]
34. Cai, S.; Zhang, D.; Shi, L.; Xu, J.; Zhang, L.; Huang, L.; Li, H.; Zhang, J. Porous Ni-Mn oxide nanosheets in situ formed on nickel foam as 3D hierarchical monolith de-NO_x catalysts. *Nanoscale* **2014**, *6*, 7346–7353. [[CrossRef](#)] [[PubMed](#)]
35. Lu, G.; Linsebigler, A.; Yates Jr, J.T. Ti^{3+} defect sites on TiO_2 (110): Production and chemical detection of active sites. *J. Phys. Chem.* **1994**, *98*, 11733–11738. [[CrossRef](#)]
36. Zhang, J.; Gao, W.; Dou, M.; Wang, F.; Liu, J.; Li, Z.; Ji, J. Nanorod-constructed porous Co_3O_4 nanowires: Highly sensitive sensors for the detection of hydrazine. *Analyst* **2015**, *140*, 1686–1692. [[CrossRef](#)] [[PubMed](#)]
37. Yan, S.; Wang, B.; Lin, Z.; Sun, B.; Pan, L.; Wu, J.; Shi, Y. Enhanced Nonenzymatic Sensing of Hydrogen Peroxide Released from Living Cells Based on Graphene Aerogel/Platinum Nanoparticle. *Sci. Adv. Mater.* **2016**, *8*, 1165–1171. [[CrossRef](#)]
38. Yagati, A.K.; Park, I.; Cho, S.; Min, J. Impedimetric Horseradish Peroxidase Sensor Based on Polyaniline-Nanofiber-Modified Microdisk Electrode Arrays. *Sci. Adv. Mater.* **2017**, *9*, 1595–1602. [[CrossRef](#)]
39. Li, J.; Lin, X. Electrocatalytic oxidation of hydrazine and hydroxylamine at gold nanoparticle—Polypyrrole nanowire modified glassy carbon electrode. *Sens. Actuators B Chem.* **2007**, *126*, 527–535. [[CrossRef](#)]
40. Pinter, J.S.; Brown, K.L.; DeYoung, P.A.; Peaslee, G.F. Amperometric detection of hydrazine by cyclic voltammetry and flow injection analysis using ruthenium modified glassy carbon electrodes. *Talanta* **2007**, *71*, 1219–1225. [[CrossRef](#)] [[PubMed](#)]
41. Yi, Q.F.; Yu, W.O. Nanoporous gold particles modified titanium electrode for hydrazine oxidation. *J. Electroanal. Chem.* **2009**, *633*, 159–164. [[CrossRef](#)]
42. Perez, E.F.; Neto, G.D.O.; Tanaka, A.A.; Kubota, L.T. Electrochemical sensor for hydrazine based on silica modified with nickel tetrasulfonated phthalocyanine. *Electroanalysis* **1998**, *10*, 111–115. [[CrossRef](#)]
43. Salimi, A.; Miranzadeh, L.; Hallaj, R. Amperometric and voltammetric detection of hydrazine using glassy carbon electrodes modified with carbon nanotubes and catechol derivatives. *Talanta* **2008**, *75*, 147–156. [[CrossRef](#)] [[PubMed](#)]
44. Li, M.; Huang, X.; Wu, C.; Xu, H.; Jiang, P.; Tanaka, T. Fabrication of two-dimensional hybrid sheets by decorating insulating PANI on reduced graphene oxide for polymer nanocomposites with low dielectric loss and high dielectric constant. *J. Mater. Chem.* **2012**, *22*, 23477–23484. [[CrossRef](#)]

